Enhancing Nighttime Power Generation: A Bionic Flower-Inspired Thermoelectric System with Photothermal Absorption and Radiative Cooling

Yue Dong, Hengtao Li, Yunxian Ji and Yinmo Xie*

School of New Energy, Harbin Institute of Technology, Weihai, 264209, China

Abstract: The combination of solar energy and radiative cooling through thermoelectric generators (TEGs) offers a promising approach for sustainable power generation. However, current thermoelectric systems that integrate solar energy and radiative cooling still face the challenge of insufficient nighttime power generation capacity. This study proposes a thermoelectric power generation system featuring a heat storage structure inspired by bionic flowers, which utilizes residual heat stored during the daytime to supply heat to the hot end of TEGs at night, thereby increasing the temperature difference at night. A numerical model was developed, and the temperature field and phase change characteristics within the heat storage structure were investigated through finite element simulation. The thermoelectric system with a heat storage structure maintains a higher nighttime voltage than the one without it. After 12 AM, the system without a heat storage structure can only sustain an output voltage of approximately 18 mV. In contrast, the system with a heat storage structure can achieve a voltage output of 42.57 mV. Even four hours later, it retained a 6.64 mV advantage. The results demonstrate that the heat storage structure significantly enhances the power generation performance at night. This research provides a potential solution to effectively mitigate the issue of insufficient nighttime power generation capacity in thermoelectric power generation systems.

Keywords: Radiative cooling, Photothermal conversion, Phase change materials, Thermoelectric power generation.

1. INTRODUCTION

Driven by industrial growth and population expansion, global energy demand has surged significantly, both stressing existing energy systems and exacerbating environmental challenges. Fossil fuels such as natural gas, coal, and oil have driven up carbon emissions, exacerbated environmental pollution, ecological damage, and global warming [1]. Therefore, developing and efficiently utilizing renewable clean energy has become critically important [2]. Among various renewable clean energy sources, solar energy possesses unique advantages: it is the most widely distributed resource, can be deployed flexibly, and can be directly and efficiently converted into electricity [3]. It stands out in terms of geographical compatibility and application universality.

Efficiently converting the sunlight that reaches the Earth into thermal energy is the most economical and environmentally friendly way to utilize solar energy. In recent years, the integration of photothermal conversion (PTC) and radiative cooling (RC) technologies has provided an innovative pathway to enhance the performance of thermoelectric generators (TEGs). TEG systems generate electricity through temperature differences, with outstanding advantages including simple structure, zero fuel consumption, zero emissions, and silent operation [4]. Notably, it has been proven that they can achieve off-grid power supply at night without batteries, showing great potential in special applications such as outdoor lighting, off-grid IoT sensors, and micro-monitoring [5].

Radiative cooling (RC) represents a sustainable, highly efficient passive cooling method requiring no additional energy input. It also serves as a crucial complementary passive thermal management technique for thermoelectric technologies, attracting significant attention for overcoming limitations of conventional cooling approaches [6, 7]. The core principle is that surface objects release their own heat in the form of electromagnetic waves through thermal radiation. By taking advantage of the high transmissivity of the atmosphere in the 8–13 μm band (the "atmospheric window"), the heat is transferred to outer space with a temperature of approximately 3K, achieving passive cooling without additional energy consumption. By utilizing the combined effect of a huge heat source based on solar energy and the cold space of the universe at 3K for TEG thermoelectric power generation, a relatively stable cold source can be used to achieve continuous power generation, and the overall energy output of the system can be effectively enhanced [8].

Previous studies have demonstrated the potential of radiative cooling to enhance TEG system performance: Gao *et al*. [9] proposed a self-powered device utilizing radiative cooling effects, introducing a selective solar absorption device between the radiative cooler and the TEG generator, enabling 24-hour continuous operation.

*Address correspondence to this author at the School of New Energy, Harbin Institute of Technology, Weihai, 264209, China;
E-mail: xieyinmo@hit.edu.cn

Received on 30-09-2025 Accepted on 01-11-2025 Published on 03-11-2025

E-ISSN: 2410-2199/25

Liu *et al*. [10] developed a novel radiative cooling-driven thermoelectric generator demonstrating significantly enhanced power generation compared to existing components—24% improvement in inland regions and 71% in coastal areas. Zhang *et al*. [11] demonstrated an adaptive system enabling vanadium dioxide (VO_2) thin films to perform thermoelectric conversion via photothermal (PT) and radiative cooling (RC) effects. During daytime, the PT mode operates with high solar absorption and low emissivity in the 8–13 μm range. At night, the TE subsystem radiates heat into the cold outer space with high emissivity. Results from the adaptive PT/RC-TE system demonstrate the potential for intelligent 24-hour energy generation without storage.

However, existing research on solar-radiative cooling-integrated thermoelectric power systems still faces challenges in insufficient nighttime power generation capacity. Therefore, we propose the following biomimetic structure to enhance nighttime power generation.

In nature, plants require sunlight absorption for growth and energy distribution to various organs. Obtaining and maintaining an optimal flower temperature is really imperative for successful plant reproduction [12]. The shape of the flower plays a crucial role in maintaining the best thermal balance. The central stamens can be heated by direct sunlight and the additional reflection of light by the petals. Meanwhile, the petals' wrapping around the central stamens forms a relatively closed ‘microgreenhouses’, effectively reducing heat loss.

Inspired by natural flowers, a biomimetic energy storage thermoelectric power generation system is proposed, as shown in Figure **1**. During the day, it enhances the absorption of solar heat through a solar heat absorption coating and simultaneously stores the absorbed solar energy in energy storage materials. The entire thermal storage tank is connected to the hot end of a thermoelectric generator (TEG). The “petal” structure (polished aluminum plates) functions as a radiative cooling reflector. The cold end of the TEG, which is covered by radiative cooling coating, emits long-wave radiation through the radiative cooling coating on its surface to exchange heat with the 3K outer space for cooling. At night, the hot end continuously releases stored latent heat from phase changes, providing a stable heat supply. The cold end continues exchanging heat with outer space. This system is expected to solve the common problem of insufficient nighttime power generation capacity in thermoelectric power generation systems by utilizing the residual heat stored during the day.

For the petal part, it serves as an infrared reflector. Polished aluminum sheets are employed, taking advantage of their excellent full-spectrum reflection properties, to reflect the energy radiated from the cold end of the TEG. Consequently, heat is efficiently dissipated into outer space through the atmospheric window, achieving cooling of the cold end. Here, the angle parameter α is introduced to represent the angle between the infrared reflector and the TEG. The transmission path of thermal radiation will vary depending on the value of α. As shown in Figure **2** [13], when the α value is small, the thermal radiation emitted by the radiative cooling coating is mainly reflected and absorbed by the device itself; while when the α value is appropriately increased, due to the size limitation of the TEG, some of its radiation cannot be effectively guided to deep space through the aluminum reflector. Therefore, the α value should neither be too small nor too large. In this study, the angle α is set at 45°, at

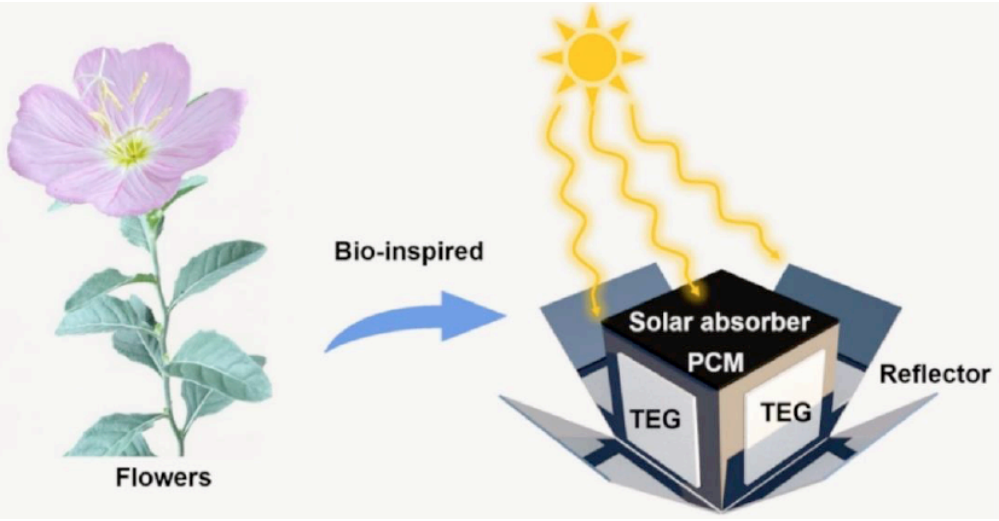

Figure 1: Chemical diagram of a thermoelectric power generation system based on a thermal storage structure.

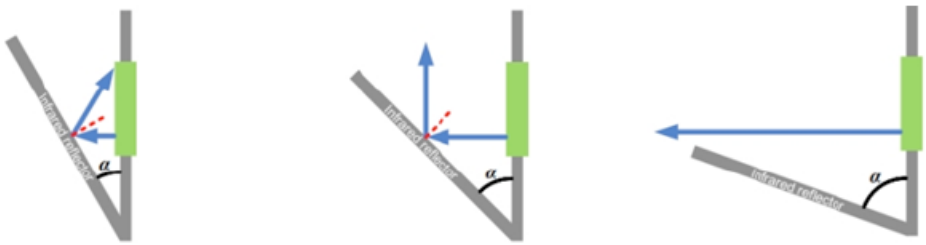

Figure 2: Selection of the Angle α between the Infrared Reflector and the TEG [13].

which point the energy can be reflected more directly to the sky, achieving a better cooling effect.

For the flower core part, it serves the functions of heat storage and power generation. On the outside of the cavity, the entire cavity is coated with a solar absorption coating. On the four sides of the cavity, TEGs are arranged to utilize the cavity as the hot end. On the other side of the TEGs, a radiative cooling coating is applied to achieve thermoelectric power generation. Inside the cavity, it is filled with PCM. For the PCM, materials with relatively low phase change temperatures can be selected. Through more latent heat of phase change, heat can be efficiently stored and provide heat for a longer time at night.

Overall, the bionic flower structure offers multiple functional advantages over conventional planar designs. Its 3D petal configuration increases the photothermal absorption surface area within the same footprint, while the angled petals optimize the radiative cooler's sky view factor. The enclosed design also helps stabilize the air layer around the hot end, reducing convective heat loss. This integrated approach synergistically enhances solar collection, radiative cooling, and thermal management, resulting in improved all-day power generation.

We first establish a numerical model of the bionic flower structure. Subsequently, based on this numerical model, mesh independence verification and model validation are conducted to ensure the model's accuracy. The temperature field and phase change characteristics within the heat storage structure are investigated, along with a comparison of the power generation performance between systems with and without the heat storage structure. It is demonstrated that the thermoelectric power generation system based on the heat storage structure has the ability to enhance the power generation performance at night.

2. METHODS

The development of numerical models involves formulating both physical and mathematical representations, specifying boundary conditions, and generating a computational mesh. To optimize computational resources while ensuring the accuracy of results, it is also necessary to verify the grid independence and the validity of the model.

2.1. Theoretical Model

2.1.1. Theoretical Model of Photo-Thermal Absorption End

The solar energy that reaches the Earth's surface arrives as thermal radiation, predominantly in the visible and near-infrared spectrum (0.3-2.5 μm), which is subsequently transformed into thermal energy upon

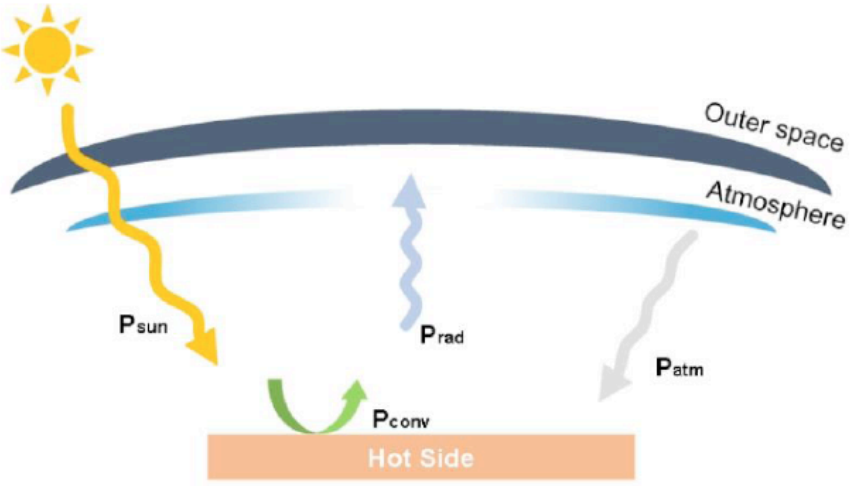

Figure 2: Schematic diagram of the energy balance on the surface of the photothermal absorption end.

absorption by materials. The heat transfer process of the photothermal absorption end can be discussed with a focus on the surface of the photothermal absorption end. The heat transfer at the solar thermal absorber comprises four components: the absorber's own emitted radiation power, $P_{rad}(T_{hot})$; the absorbed atmospheric radiation power, $P_{atm}(T_{amb})$; the absorbed solar radiation power, $P_{sun,hot}$; and the convective heat transfer power with the ambient environment, $P_{conv,hot}$.

According to the principle of radiative heat transfer, the thermal radiation power (P_{rad}) of the solar thermal absorption end is related to its radiation characteristics and surface temperature. The expression for this relationship is as follows:

$$P_{rad}(T)=\int_0^{\infty}\int_{\Omega} I(\lambda,\theta,\varphi,T)\cos\theta d\omega d\lambda \tag{1}$$

Where $I(\lambda,\theta,\varphi,T)$ denotes the spectral directional emissive power of the surface at the photothermal absorption end. λ、θ, *and* φ denote the wavelength, latitude angle, and longitude angle, respectively. The relationship between solid angle and longitude and latitude angles is as follows:

$$d\omega=\sin\theta d\theta d\varphi \tag{2}$$

According to the definition of spectral directional emissivity, the spectral directional emissive power $I(\lambda,\theta,\varphi,T)$ emitted from a radiator surface can be expressed as:

$$I(\lambda,\theta,\varphi,T)=\varepsilon(\lambda,\theta,\varphi,T)\cdot I_{BB}(\lambda,T) \tag{3}$$

Among these, $\varepsilon(\lambda,\theta,\varphi,T)$ denotes the spectral directional emissivity of the radiator, while $I_{BB}(\lambda,T)$ represents the spectral radiant power of a blackbody at temperature T, determined by Planck's radiation law, specifically:

$$I_{BB}(\lambda,T)=\frac{2h_0c_0^2}{\lambda^5 e^{h_0c_0/(\lambda k_0 T)}-1} \tag{4}$$

Where h_0 denotes Planck's constant, k_0 represents Boltzmann's constant, and c_0 signifies the speed of light in vacuum. It can be sorted out as follows:

$$P_{rad}(T_{hot})=\int_0^{\infty}\int_0^{2\pi}\int_0^{\pi/2}\varepsilon(\lambda,\theta,\varphi,T)I_{BB}(\lambda,T)\cos\theta\cdot\sin\theta\cdot d\theta d\varphi d\lambda \tag{5}$$

The emissivity of the photothermal absorber (ε_{hot}) is assumed constant, governed by its material properties. Additionally, for most practical surfaces, the influence of the longitudinal angle on surface emissivity can be disregarded [14]. For the photothermal absorption end surface, ε_{hot} denotes the emissivity of the surface of the photothermal absorption end, and its thermal radiation power is given by:

$$P_{rad}(T_{hot})=2\pi\int_0^{\infty}\int_0^{\pi/2}\varepsilon_{hot}(\lambda,\theta)I_{BB}(\lambda,T_{hot})\cos\theta\cdot\sin\theta\cdot d\theta d\lambda \tag{6}$$

Photothermal absorber surfaces not only emit radiation outward but also receive radiation from the atmosphere onto their surfaces, which can be expressed as follows:

$$P_{atm}(T_{amb})=2\pi\int_0^{\infty}\int_0^{\pi/2}\varepsilon_{hot}(\lambda,\theta)\varepsilon_{atm}(\lambda,\theta)I_{BB}(\lambda,T_{amb})cos\theta\cdot sin\theta\cdot d\theta d\lambda \tag{7}$$

Here, $\varepsilon_{atm}(\lambda,\theta)$ denotes the equivalent spectral directional emissivity of the atmosphere, and T_{amb} represents the ambient temperature.

Previous research indicates [15] that the solar radiation power exceeds the net cooling power from sky radiation by approximately one order of magnitude. Therefore, most of the energy at the surface of the photothermal absorption end comes from solar radiation, which causes an increase in the temperature of the photothermal absorption surface. The two commonly employed standard spectral distributions are 'Extraterrestrial AM1.5' and 'Global tilt AM1.5'. The former refers to the solar spectrum measured outside the atmosphere, while the latter is the spectrum measured on a tilted surface on the ground, accounting for the effects of atmospheric absorption, scattering, and other factors, thus more accurately reflecting actual solar radiation conditions in applications. Consequently, this article adopts the Global tilt AM1.5 spectral curve. The solar radiation power absorbed at the solar thermal absorber end, $P_{sun,hot}$, is given by:

$$P_{sun,hot}=2\pi\int_0^{\infty}\int_0^{\pi/2}\varepsilon_{hot}(\lambda,\theta)I_{AM1.5}(\lambda)cos\theta\cdot sin\theta\cdot d\theta d\lambda \tag{8}$$

In addition, during the heat transfer process, at the photothermal absorption end, the absorber surface temperature exceeds the ambient temperature due to the absorbed solar radiation energy. This readily induces convective heat exchange between the surrounding ambient air and the absorber surface, thereby reducing the absorber temperature. To simplify convective heat exchange in this study, a comprehensive heat transfer coefficient is employed to relate the temperature difference between the solar thermal absorber and the ambient air, serving as the convective heat transfer power of the solar thermal absorber. The expression is:

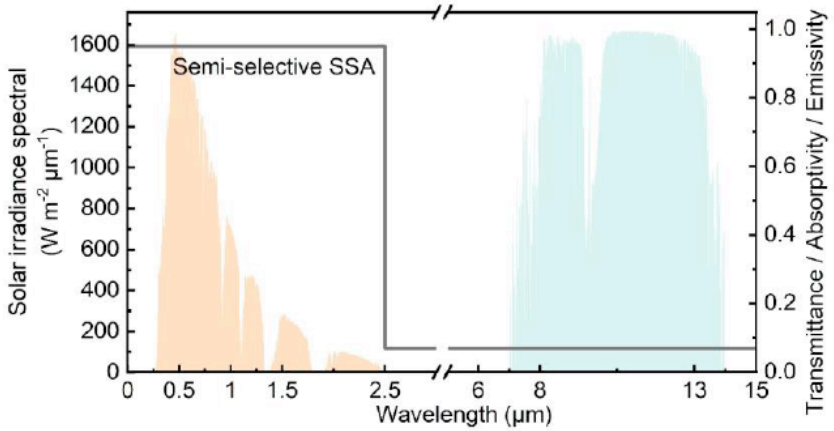

Figure 3: Ideal Selective Photothermal Absorption Coating.

$$P_{conv,hot} = h_h \cdot (T_{hot} - T_{amb}) \quad (9)$$

Among them, h_h is the comprehensive heat transfer coefficient between the heat absorption end and the surrounding environment.

To maximize solar energy utilization and minimize radiative heat loss through the atmospheric window, the photothermal absorber must exhibit high spectral selectivity. Specifically, it requires high absorptivity (emissivity) within the solar spectrum (0.3–2.5 μm) and low emissivity in the mid-infrared range (2.5–15 μm) to suppress its own thermal radiation. Figure **3** shows an ideal selective absorption coating.

2.1.2. Theoretical Model of the Radiative Cooling End

The heat exchange at the radiative cooler surface is governed by four distinct power components: the emitted thermal radiation, $P_{rad}(T_{prc})$; the absorbed atmospheric radiation, $P_{atm}(T_{amb})$; the absorbed solar radiation, $P_{sun,prc}$; and the convective heat transfer with the ambient environment, $P_{conv,prc}$.

Similarly, the thermal radiation power emitted by the radiative cooling end itself is $P_{rad}(T_{prc})$:

$$P_{rad}(T_{prc}) = 2\pi \int_0^{\infty} \int_0^{\pi/2} \varepsilon_{prc}(\lambda,\theta) I_{BB}(\lambda, T_{prc}) \cos\theta \cdot \sin\theta \cdot d\theta \cdot d\lambda \quad (10)$$

T_{prc} and ε_{prc} denote the radiative cooling end surface temperature and its surface emissivity, respectively.

The specific expression for $\varepsilon_{atm}(\lambda,\theta)$ will be expressed for both the 'atmospheric window' and 'non-atmospheric window' wavelength ranges[16], with the expression being:

$$\varepsilon_{atm}(\lambda,\theta) = \begin{cases} 1 & (\lambda < 8\mu m, \lambda > 13\mu m) \\ 1 - [1 - \varepsilon_{atm}(\lambda, 0)]^{1/cos\theta} & (8\mu m < \lambda < 13\mu m) \end{cases} \quad (11)$$

$\varepsilon_{atm}(\lambda,0)$ denotes the spectral absorption in the vertical direction of the atmosphere. The atmospheric radiation power absorbed by a radiatively cooling surface is given by:

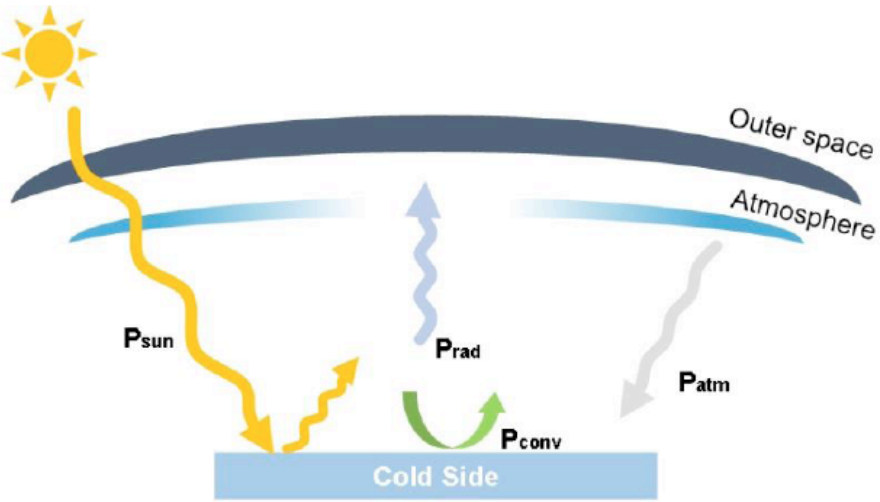

Figure 4: Schematic Diagram of the Energy Balance on the Surface of the Radiative Cooling End.

$$P_{atm}(T_{amb}) = 2\pi \int_0^{\infty} \int_0^{\pi/2} \varepsilon_{cold}(\lambda,\theta)\varepsilon_{atm}(\lambda,\theta) I_{BB}(\lambda,T_{amb}) cos\theta \cdot sin\theta \cdot d\theta d\lambda \quad (12)$$

The radiative cooling surface will also receive a portion of solar radiation:

$$P_{sun.prc} = 2\pi \int_0^{\infty} \int_0^{\pi/2} \varepsilon_{prc}(\lambda,\theta) I_{AM1.5}(\lambda) cos\theta \cdot sin\theta \cdot d\theta d\lambda \quad (13)$$

In addition, during the heat transfer process at the radiative cooling end, due to the radiative cooling end being located at both ends of the TEG, the photothermal end has absorbed solar radiation energy. The TEG itself acts as a thermal resistance; the temperature at the radiative cooling end is slightly higher than the ambient temperature. This readily induces convective heat transfer between the surrounding ambient air and the surface of the radiative cooling end. Similarly, simplified convective heat transfer is employed, using a combined heat transfer coefficient that relates the temperature difference between the radiative cooling end and the ambient air to represent the convective heat transfer power at the radiative cooling end. The expression is:

$$P_{conv,cold} = h_c \cdot (T_{prc} - T_{amb}) \quad (14)$$

2.1.3. Theoretical Model of Thermoelectric Power Generation

A temperature gradient exists between the hot and cold ends due to the energy conversion and heat flow. This gradient drives a heat flux, which, according to Fourier's law, is given by:

$$q = K(T_{hot} - T_{prc}) \leftarrow \quad (15)$$

The Peltier effect occurs at the junction of the thermocouple arms. The Peltier heat released on the hot side and absorbed on the cold side are respectively:

$$P_{peltier,hot} = SIT_{hot} \quad (16)$$

$$P_{peltier,prc} = SIT_{hot} \quad (17)$$

In the above equation, S represents the Seebeck coefficient of the TEG, K is the overall thermal conductivity, I is the loop current, and T_{hot} and T_{prc} are the temperatures at the hot and cold ends of the TEG, respectively.

In this study, for the sake of simplifying the analysis, the Thomson effect is ignored, and it is assumed that the Joule heat generated within the thermocouple arms is uniformly distributed between the hot and cold junctions. Based on this assumption, the heat flows Q_{hot} and Q_{cold} between the thermocouple module and the high-temperature heat source and the low-temperature heat source, respectively, are:

$$Q_{hot} = SIT_{hot} + K(T_{hot} - T_{prc}) - \frac{1}{2}I^2R \quad (18)$$

$$Q_{cold} = SIT_{prc} + K(T_{hot} - T_{prc}) + \frac{1}{2}I^2R \quad (19)$$

According to the Seebeck effect, the electrical potential difference across the two ends of a thermoelectric generator is directly proportional to the temperature difference, as expressed by:

$$U = \boldsymbol{S}(T_{hot} - T_{prc}) \quad (20)$$

According to the equation relating voltage and power, we have:

$$P_{out} = \left(\frac{U}{R + R_L}\right)^2 R_L/A_c = \left(\frac{S\Delta T}{R + R_L}\right)^2 R_L/A_c \quad (21)$$

Here, R denotes the total resistance of the thermoelectric arms inside the TEG, R_L denotes the outer resistance, and A_c denotes the surface area of the TEG. Maximizing **Equation (21)** yields the optimal

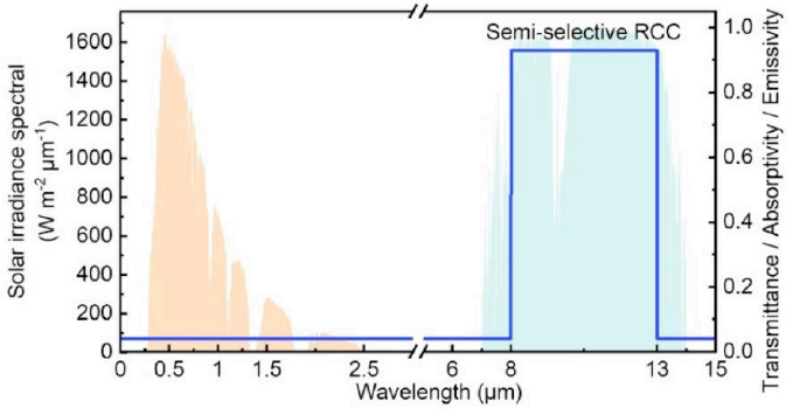

Figure 5: Spectrum of the Ideal Radiative Cooling Coating.

value of P_{out}. When the internal resistance R of the TEG is equal to the load resistance R_L, the maximum value of P_{out} is given by

$$P_{\max,\text{out}} = \frac{(S\Delta T)^2}{4RA_c} = \frac{U^2}{4RA_c} \tag{22}$$

2.1.4 Phase Transition Model

This study uses the equivalent heat capacity method to address the nonlinear problem of heat transfer during the transition process. PCM is treated as a single-phase flow. The distinction between solid and liquid is made by defining their physical parameters. In the paste zone of solid-liquid coexistence, these parameters are interpolated between the two phases to determine the fluid characteristics. Heat absorbed or released during phase transitions is included as an apparent heat capacity term in the model.

The numerical model for solving the flow field based on the fundamental equations of fluid mechanics, the continuity equation, and the Navier-Stokes equation, is expressed as **Equation (23)** and **Equation (24).**

$$\frac{\partial \rho}{\partial t} + \nabla \bullet (\rho \boldsymbol{u}) = 0 \tag{23}$$

$$\rho \frac{\partial \boldsymbol{u}}{\partial t} + \rho(\boldsymbol{u} \cdot \nabla)\boldsymbol{u} + \nabla P - \nabla\left[\mu\left(\nabla \boldsymbol{u} + (\nabla \boldsymbol{u})^T\right)\right] = F_v + F_b \tag{24}$$

Here, ρ denotes density, P denotes pressure, *μ* denotes dynamic viscosity, and *u* denotes velocity. The continuity equation ensures mass conservation, while the Navier-Stokes equations control fluid motion. The first two terms in **Equation (24)** represent inertial forces, and the third term represents the pressure term. The right-hand side of the equation represents the external forces acting upon the PCM. Based on the Boussinesq approximation, the buoyancy required for natural convection when the fluid phase is in the liquid state is given, where gravitational acceleration g is 9.81 m/s², and *β* is the thermal expansion coefficient:

$$F_b = g\beta p_l (T - T_{pc}) \tag{25}$$

The expression for the volume force in the momentum equation used to calculate the velocity of PCM in the solid or liquid state is:

$$F_v = -A(T) \bullet \boldsymbol{u} \tag{26}$$

In the equation, *u* denotes the fluid velocity (considered static with zero velocity in the solid state). The concept of porosity can be employed to modify the continuity equation to define the fluid properties within the paste zone. To describe convective behaviour within the liquid phase, the enthalpy-porosity method is available. Furthermore, within the flow through the porous media, the momentum equation in the paste region may be simulated using the *Carman-Kozeny* equation with the porosity function *A*(*T*) to characterise the flow characteristics further.

$$A(T) = A_{mush} \frac{(1-\Omega)^2}{(\Omega^3 + \Phi)} \tag{27}$$

A_{mush} is associated with porous media and controls convective heat transfer in the paste region. Its value typically ranges 10^4-10^8kg·m^{-3}s^{-2}, and in this study, it is set to 10^6[17]. The purpose of introducing Φ is to prevent *A*(*T*) from tending towards infinity when the liquid fraction is zero. Assuming Φ=0.001 ensures the stability of numerical calculations. The phase transition is characterised by the phase separation fraction Ω, defined as shown in **Equation (28)**. The phase transition temperature range parameter ΔT_{pc} is used to determine the temperature interval of the phase transition region:

$$\Omega(T) = \begin{cases} 0, & T < T_{pc} - \dfrac{\Delta T_{pc}}{2} \\ \dfrac{T - \left(T_{pc} - \frac{\Delta T_{pc}}{2}\right)}{\Delta T_{pc}}, & T_{pc} - \dfrac{\Delta T_{pc}}{2} \le T \le T_{pc} + \dfrac{\Delta T_{pc}}{2} \\ 1, & T > T_{pc} + \dfrac{\Delta T_{pc}}{2} \end{cases} \tag{28}$$

In the liquid phase region with phase separation fraction Ω(*T*)=1, the value of the source term *A*(*T*) approaches zero, and the fluid flow behaviour may be regarded as following the standard *Navier-Stokes* equations. In contrast, within the solid phase region and the transition zone between solid and liquid phases, the phase separation fraction satisfies Ω(*T*)<1. Here, the value of the source term *A*(*T*) increases significantly, its magnitude being determined by the paste factor A_{mush}. Due to the influence of this source term, fluid flow is blocked in the solid phase region and reduced in the transition zone between the solid and liquid phases.

When the phase change material (PCM) begins to melt, the influence of fluid flow (*i.e.*, velocity) on the heat transfer process needs to be considered in the momentum equation. To comprehensively describe the impact of convective effects in all phases, a viscosity parameter that varies with temperature is introduced to characterize the fluid's flow characteristics under different temperature conditions.

$$\mu(T) = \mu_l (1 + A(T)) \tag{29}$$

When the liquid phase fraction is zero, it can be known that the viscosity at this time is extremely high, and the system is regarded as a static fluid. In the liquid state, the viscosity is defined as 0.008 $kg \cdot m^{-1} \cdot s^{-1}$. The model defines equivalent thermal conductivity and equivalent density for the solid-liquid two-phase region, where the subscripts s and l denote the solid phase and liquid phase, respectively:

$$k_{eff} = \Omega k_l + (1 - \Omega) k_s \tag{30}$$

$$\rho_{eff} = \Omega \rho_l + (1 - \Omega) \rho_s \tag{31}$$

The equivalent heat capacity method describes phase transition processes using modified specific heat capacities. This method introduces latent heat of phase transition into the energy conservation equation as modified specific heat capacities, thus avoiding the complexity of explicitly handling latent heat terms. Specifically, latent heat acts as a thermal physical parameter during phase transitions, and its release or absorption is described by a Gaussian function characterized by the phase transition temperature T_{pc}, as shown mathematically in **Equation (32)**. This method smoothly captures the nonlinear variation of material thermal properties within the phase transition temperature range. It improves the stability and convergence of numerical simulations and can be applied to solving phase transition heat transfer problems.

$$D(T) = \frac{e^{-\frac{(T - T_{pc})^2}{(\Delta T_{pc}/4)^2}}}{\sqrt{\pi (\Delta T_{pc}/4)^2}} \tag{32}$$

The apparent heat capacity is the sum of the equivalent heat capacity and the phase change latent heat, with *L* being the latent heat of phase change and c_p being the specific heat capacity:

$$c_p(T) = c_{p,s} + \Omega(T) \cdot (c_{p,l} - c_{p,s}) + L \cdot D(T) \tag{33}$$

2.2. Model Description

The geometric model and dimensions constructed in the finite element simulation are shown in Figure **6**. It includes an aluminum cavity and PCM (phase change materials) within the cavity. TEG is attached to the cavity, allowing heat to be transferred to its hot end. A combination of radiative cooling coating and reflectors provides radiative cooling to the cold ends of the TEGs.

The specific physical properties of PCM are shown in the following Table **1**:

For this study, the boundary and initial values were set as follows: thermal insulation boundary conditions were applied to the bottom of the PCM cavity and the periphery of the TEG ceramic substrate. Natural convection heat transfer occurred at the walls, with an initial potential of zero. The copper plate at the TEG tail

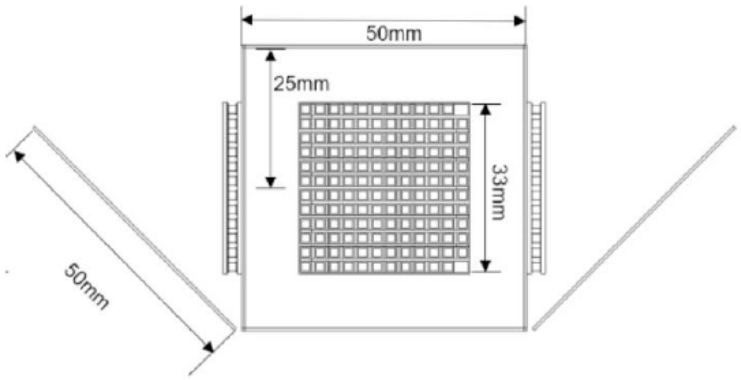

Figure 6: Schematic diagram of geometric model.

Table 1: Thermal Physical Parameters of Phase Change Paraffin RT28HC

RT28HC Physical Parameters	Values
Density ($kg \cdot m^{-3}$)	880(solid), 770(liquid)
Phase change latent heat ($kJ \cdot kg^{-1}$)	250
Phase Change Temperature (K)	301
Phase Change Interval (K)	4
Thermal Conductivity ($W \cdot m^{-1} \cdot K^{-1}$)	0.2
Specific Heat Capacity ($J \cdot kg^{-1} \cdot K^{-1}$)	2390(solid), 2180(liquid)
Volume of PCM (mm^3)	49.5×49.5×49.5

end was grounded. The upper surface of the TEG and the cavity surface were designated as opaque surfaces.

2.3. Grid Independence Verification

To balance computational accuracy and efficiency, a grid independence study was conducted. The objective was to identify a mesh configuration that achieves sufficient precision with minimal cell count. Several mesh densities were evaluated, ranging from 68,324 to 1,017,845 cells. The volume temperature of the PCM and the temperature difference between the two ends of the TEG were selected as benchmark parameters. The verification results are shown in Figure **7**. When the two curves stabilize, it indicates that further increasing the number of grids has a negligible effect on the computational results. Therefore, 615,734 grid cells were determined for subsequent calculations and analysis.

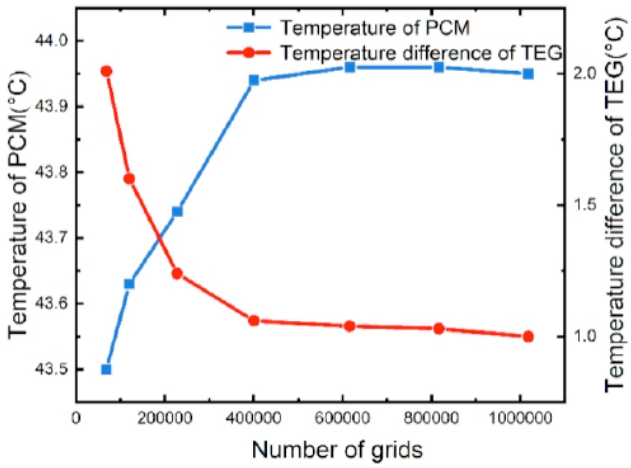

Figure 7: Results diagram of grid independence verification.

2.4. Model Verification

The model's accuracy was validated against reference [18] in two key aspects: solar radiation and PCM phase change. Figure **8a)** depicts the variation of the solar absorber temperature at the system top over time, while Figure **8b)** illustrates the variation of the PCM temperature within the system over time. The root mean square error (RMSE) for Figure **8a)** and Figure **8b)** is 1.67K and 1.93K, respectively. This indicates that the simulation results agree well with the literature results, verifying the accuracy of the established model.

3. RESULTS AND DISCUSSIONS

3.1. Temperature Field and Phase Change Characteristics within the Heat Storage Structure

In this subsection, the variations of the internal temperature field distribution and phase change characteristics in the heat storage structure over time are presented. The simulation period spans from 8:00 AM on June 1, 2024, to 8:00 AM the following day, utilizing meteorological data from Weihai, Shandong Province, China, for environmental conditions. As observed in the phase-change and temperature nephograms, the solar-absorbing coating starts to absorb energy after only 0.1 hours of solar radiation, consistent with its high absorption efficiency within the solar wavelength range. Through thermal conduction, this heat is transferred to the aluminum shell, causing the PCM near the aluminum shell to heat up first. After another 0.4 hours, the melting zone of the phase change material (PCM) near the aluminum shell continues to expand. The nephogram shows a noticeable temperature increase near the shell, spreading radially inward and causing more areas to enter the phase change stage. However, due to the low thermal conductivity of PCM, the central region remains relatively cool and has not yet completed significant melting. At this stage, the heat storage unit gradually heats up from the outside to the inside, undergoing phase transitions that create significant temperature gradients and phase transition gradients. Cross-sectional temperature distributions reveal that

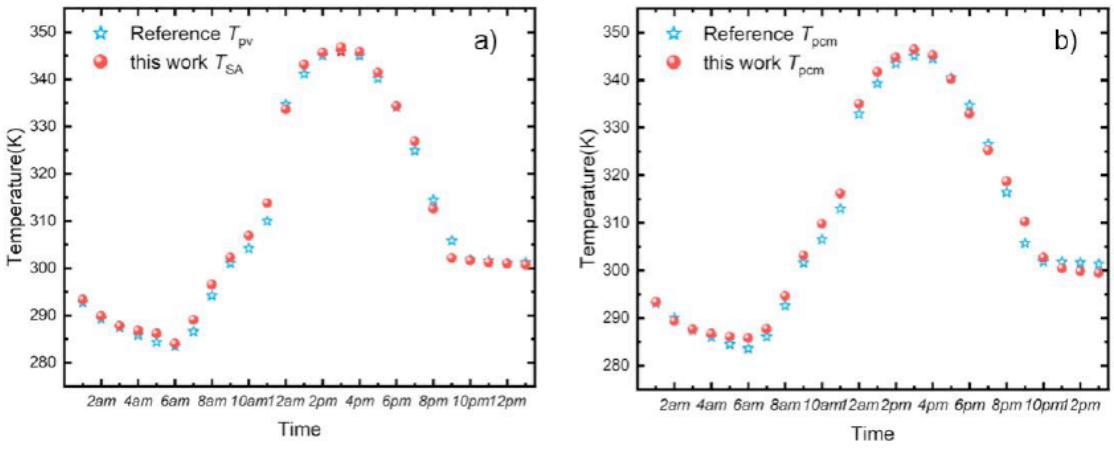

Figure 8: Model verification against Yusuf's results [18].

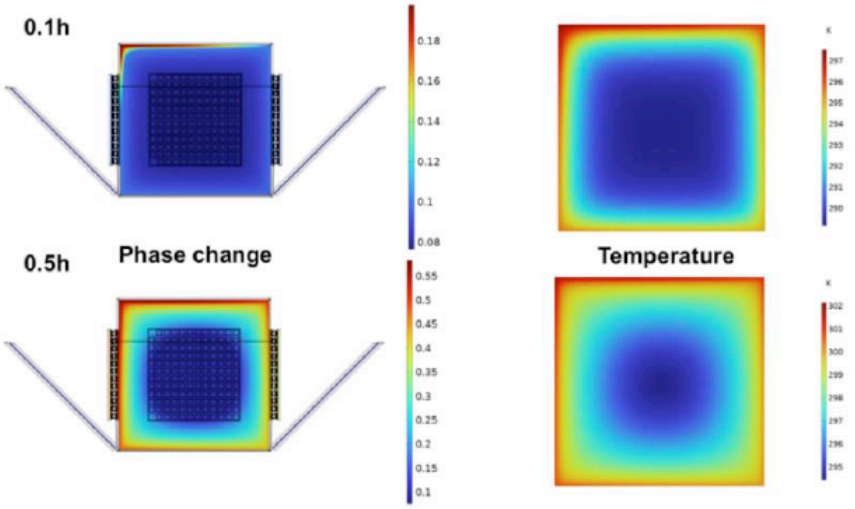

Figure 9: Phase change status (**left**) and temperature distribution (**right**) at 0.1 h and 0.5 h from 8:00 AM.

phase change first occurs in the upper-left region, with temperatures slightly higher on the left side than the right. This phenomenon is primarily attributed to irradiation asymmetry caused by the solar azimuth angle. This asymmetry results in relatively greater effective radiation received on the left side, thereby promoting local temperature rise and accelerating the initiation of the phase change process.

After about 3.7 hours of heating by the sun's rays, the phase change material (PCM) near the outer region of the aluminum shell has largely melted, while the central area remains at a lower temperature and has not yet fully entered the phase change stage. The phase change nephogram revealed a distinct annular boundary between the melted and unmelted regions. The temperature nephogram indicated higher temperatures at the periphery, gradually decreasing and spreading radially toward the center, forming a pronounced temperature gradient. After an additional 0.6 hours, the phase change nephogram showed only a small amount of solid phase remaining in the central region, with the peripheral area having largely completed the phase change. The temperature nephogram indicates a more uniform overall temperature distribution, though a certain temperature gradient persists in the central region. The heat absorption coating absorbs heat, with part of it transferred to the PCM to heat and promote its phase change, and another part of the heat is transferred to the hot end of the TEG through tangential heat conduction. Subsequently, as the cold end of the TEG undergoes radiative cooling, a sustained temperature difference is established across the device. This growing thermal gradient results in a continuous rise in the TEG's output voltage.

After 4.3 hours of solar irradiation, the phase change material (PCM) had largely completed melting. By 10.4 hours, the phase change cloud map was

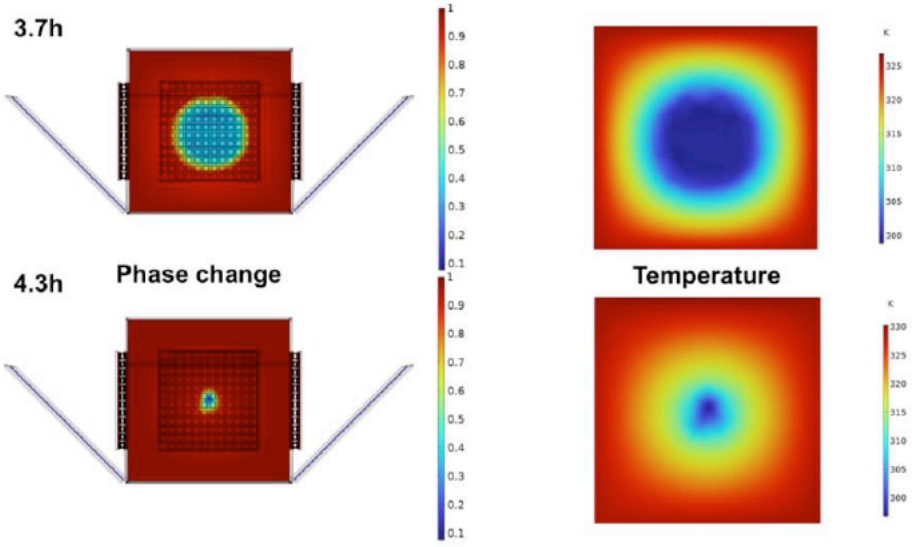

Figure 10: Phase change status (**left**) and temperature distribution (**right**) at 3.7h and 4.3h from 8:00 AM.

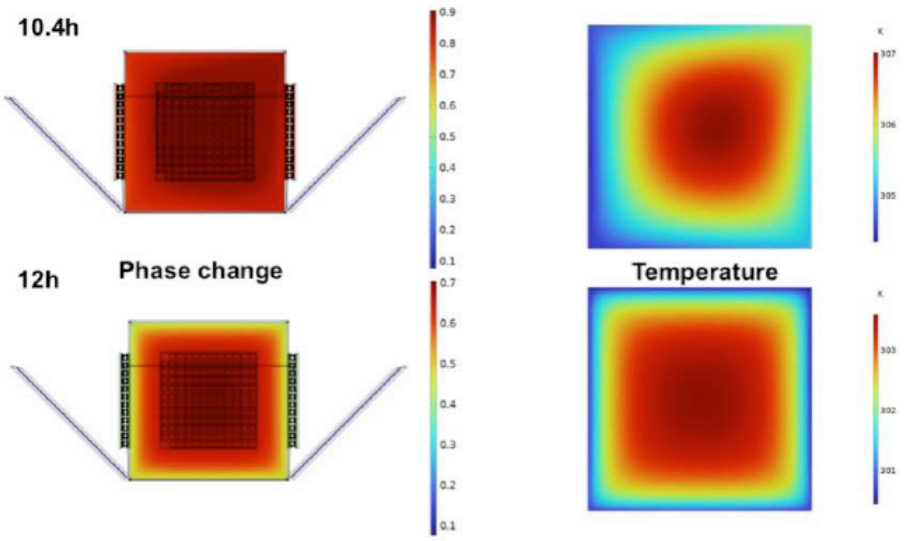

Figure 11: Phase change status (**left**) and temperature distribution (**right**) at 10.4 h and 12h from 8:00 AM.

almost entirely red, indicating that the material had persisted in a liquid state. This demonstrates that during hot summer months, the PCM can remain in a melted state from noon until 6 PM. Under the combined influence of solar radiation and ambient temperature during this period, the thermal nephogram shows a uniform temperature distribution within the storage unit. This uniformity creates favorable thermal conditions for sustained and stable heat release throughout the night. After 10.4 hours, the uneven temperature distribution in the nephogram shifted from the upper left to the upper right, corresponding to the change in the sun's azimuth. During this period, while the PCM interior was still undergoing phase change, the combined decrease in both solar intensity and ambient temperature initiated a cooling process at the aluminum shell surface. Consequently, heat began to gradually transfer outward from the PCM. However, residual sunlight around 18:00 (after 12h) delayed the cooling of the shell edges.

As solar radiation gradually decreases, the system enters the nighttime period without sunlight. The PCM begins to release heat to its surroundings and starts the transition from the liquid to the solid phase. The phase-change nephogram after 12h indicates that solidification first occurs in areas with lower external temperatures. A distinct cooling trend is observable in the temperature nephogram, confirming the initiation of the heat release process. This ensures the system maintains a certain level of power generation capability even under conditions without solar radiation. After about seven hours of heat release, as shown in Figure **12**, the phase-change nephogram cloud map after 19.3h indicates that a large area inside the PCM has solidified, with only a local region in the center still not completely phase changed.

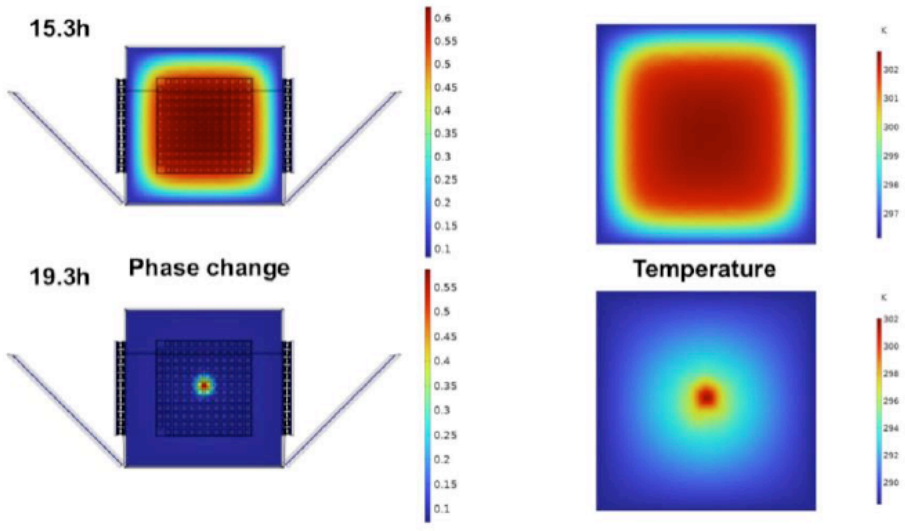

Figure 12: Phase change status (**left**) and temperature distribution (**right**) at 15.3 h and 19.3h from 8:00 AM.

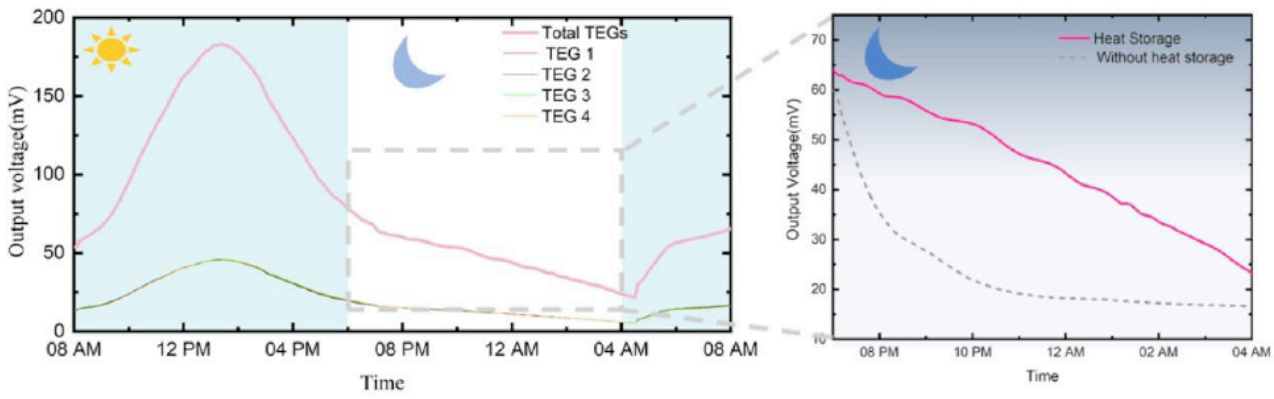

Figure 13: 24-hour power generation performance of the thermoelectric power generation system with a heat storage structure.

3.2. 24-Hour Power Generation Performance with Integrated Thermal Storage

Figure **13** shows the performance of thermoelectric power generation with a heat storage system, comparing the impact of having or not having a heat storage structure on the nighttime power generation performance. To comprehensively evaluate the system's power generation capabilities, its voltage output was monitored throughout the entire day. Four TEGs were arranged around the thermal storage cavity and connected in series to calculate the total voltage. Results indicate that as solar irradiance intensity fluctuates, the TEG output voltage exhibits a trend of first increasing and then decreasing, peaking around 13:00 with a maximum system output voltage of 196.35 mV. During nighttime conditions, the thermoelectric power generation system equipped with a thermal storage structure (PCM) demonstrated superior performance. To further quantify and analyse the impact of thermal storage structure on overall system performance, a comparison model was established in this study: the thermal storage material (PCM) was replaced with the same material as the shell. It is noteworthy that the aluminum block in the control case also provides a certain degree of thermal buffering due to its sensible heat capacity. However, the thermal discharge characteristics of sensible heat storage differ fundamentally from those of latent heat storage. The aluminum block experiences a continuous decline in temperature as it releases heat, leading to a rapidly diminishing temperature difference across the TEG. In contrast, the PCM leverages the latent heat of fusion during its solidification process, which enables it to release a large amount of energy while maintaining a relatively stable temperature plateau. This fundamental difference in thermal energy release profile is the primary reason for the more stable and prolonged voltage output observed in the system equipped with the PCM during the nighttime hours. Therefore, the enhanced performance can be attributed to the intrinsic property of latent heat storage, rather than mere thermal mass. Comparative experimental results indicate that when entering night-time conditions, the voltage of the system without thermal storage rapidly decreased, while the system with thermal storage maintained a higher voltage output. After 12:00 AM, the system without a thermal storage structure maintained an output voltage of approximately 18mV. This was primarily attributed to the radiative cooling effect on the cold-side surface during night-time, keeping the TEG cold-side temperature consistently below the ambient temperature. In contrast, the system equipped with a thermal storage structure (PCM) achieved a voltage output of 42.57 mV at 12 AM. Although its voltage subsequently decreased gradually over time, after four hours, its output remained approximately 6.64 mV higher than that of the comparison group. These results indicate that the thermal storage structure significantly mitigates the rate of heat source temperature decline during nighttime hours, maintaining a more stable temperature gradient. This demonstrates a pronounced enhancement in nighttime power generation performance.

This numerical study serves as a proof-of-concept, yet several practical challenges require attention for real-world implementation. The long-term durability of specialized coatings under environmental exposure needs verification. The economic viability of scaling up PCM usage and system sensitivity to off-design conditions like cloud cover and wind also warrant further investigation. Addressing these limitations through experimental validation will be the focus of subsequent research.

4. CONCLUSIONS

This work presents a bionic flower-inspired thermoelectric system. It mitigates the limited nocturnal performance of solar–radiative cooling systems. By storing solar heat in the daytime and releasing it at night, the system maintains the TEG's hot-end temperature and enhances the thermal gradient. A comprehensive numerical model was developed to simulate the coupled heat transfer, phase change, and

power generation processes. The following conclusions were drawn:

(1) A numerical simulation model of the thermoelectric power generation system integrated with a thermal storage structure was established, capable of accurately simulating the phase change process and temperature variation within the thermal storage structure. The validity of the model was confirmed through verification.

(2) The phase change nephogram and temperature field inside the thermal storage structure at different time points were analyzed. By evaluating the 24-hour power generation performance, it was demonstrated that the proposed structure can effectively mitigate the issue of insufficient power generation capacity of the thermoelectric system at night.

CONFLICTS OF INTEREST

The authors declare no conflict of interest.

REFERENCES

[1] Lv S, Zhang M, Tian J, *et al*. Performance analysis of radiative cooling combined with photovoltaic-driven thermoelectric cooling system in practical application. Energy, 2024, 294: 130971. https://doi.org/10.1016/j.energy.2024.130971

[2] Zhang W W, Guo Y M, He M J, *et al*. Self-adaptive photothermal/radiative cooling-thermoelectric conversion system for 24 h electricity generation. Applied Thermal Engineering, 2024, 243: 122603. https://doi.org/10.1016/j.applthermaleng.2024.122603

[3] Wang G, Zhang Z, Lin J. Multi-energy complementary power systems based on solar energy: A review. Renewable and Sustainable Energy Reviews, 2024, 199: 114464. https://doi.org/10.1016/j.rser.2024.114464

[4] Yang Z, Wang F, Fu Z, *et al*. Thermoelectric system investigation with the combination of solar concentration, greenhouse and radiative cooling for all-day power generation. Renewable Energy, 2024, 231: 120903. https://doi.org/10.1016/j.renene.2024.120903

[5] Liu M, Li X, Li L, *et al*. Sustainable all day thermoelectric power generation from the hot sun and cold universe. Small, 2024, 20(35): 2403020. https://doi.org/10.1002/smll.202403020

[6] Zhao B, Hu M, Ao X, *et al*. Radiative cooling: A review of fundamentals, materials, applications, and prospects. Applied energy, 2019, 236: 489-513. https://doi.org/10.1016/j.apenergy.2018.12.018

[7] Li Z, Chen Q, Song Y, *et al*. Fundamentals, materials, and applications for daytime radiative cooling. Advanced Materials Technologies, 2020, 5(5): 1901007. https://doi.org/10.1002/admt.201901007

[8] Mousavi S A A, Aghakhani H, Baghapour B, *et al*. Integrating radiative cooling and thermoelectric: A comprehensive review. Renewable and Sustainable Energy Reviews, 2025, 222: 115946. https://doi.org/10.1016/j.rser.2025.115946

[9] Gao K, Yang J, Shen H, et al. Uninterrupted Self□Generation Thermoelectric Power Device Based on the Radiative Cooling Emitter and Solar Selective Absorber. Solar RRL, 2022, 6(2): 2100975. https://doi.org/10.1002/solr.202100975

[10] Liu J, Zhang J, Yuan J, *et al*. Model development and performance evaluation of thermoelectric and radiative cooling module to achieve all-day power generation. Solar Energy Materials and Solar Cells, 2021, 220: 110855. https://doi.org/10.1016/j.solmat.2020.110855

[11] Zhang W W, Guo Y M, He M J, *et al*. Self-adaptive photothermal/radiative cooling-thermoelectric conversion system for 24 h electricity generation. Applied Thermal Engineering, 2024, 243: 122603. https://doi.org/10.1016/j.applthermaleng.2024.122603

[12] Van der Kooi C J, Kevan P G, Koski M H. The thermal ecology of flowers. Annals of Botany, 2019, 124(3): 343-353. https://doi.org/10.1093/aob/mcz073

[13] Xie Y M, Ji Y X, Jing W, *et al*. A high-performance all-day vertical thermoelectric generator based on a double-sided reflective structure. Case Studies in Thermal Engineering, 2024, 63: 105333. https://doi.org/10.1016/j.csite.2024.105333

[14] Bergman T L. Fundamentals of heat and mass transfer. John Wiley & Sons, 2011

[15] Li W, Fan S. Radiative cooling: harvesting the coldness of the universe. Optics and Photonics News, 2019, 30(11): 32-39. https://doi.org/10.1364/OPN.30.11.000032

[16] Lushiku E M, Hjortsberg A, Granqvist C G. Radiative cooling with selectively infrared‐emitting ammonia gas. Journal of Applied Physics, 1982, 53(8): 5526- 5530. https://doi.org/10.1063/1.331487

[17] Nouira M, Sammouda H. Numerical study of an inclined photovoltaic system coupled with phase change material under various operating conditions. Applied Thermal Engineering, 2018, 141: 958-975. https://doi.org/10.1016/j.applthermaleng.2018.06.039

[18] Yusuf A. Continuous 24-h power generation: Integrating radiative cooling with photovoltaic-phase change material-thermoelectric system. Solar Energy, 2024, 269: 112370. https://doi.org/10.1016/j.solener.2024.112370

https://doi.org/10.31875/2410-2199.2025.12.10